scientific reports

Check for updates

OPEN

Seismic energy from small earthquakes maps fault segmentation in the Southeastern Alps

M. Picozzi[1,5]✉, L. Cataldi[1], A. Viganò[2], G. Ferretti[3], P. Brondi[1], D. Bindi[4], A. Magrin[1], G. D. Chiappetta[1], A. G. Iaccarino[5], D. Scafidi[3], P. Comelli[1] & D. Spallarossa[3]

Fault strength spatial variability controls how earthquakes initiate, propagate, and arrest, yet remains poorly resolved in complex tectonic settings. The southeastern Alps constitute one of the most seismically hazardous regions in Central Europe, with active fault systems, a history of damaging earthquakes, and ongoing tectonic deformation. We analyze more than 9,200 small-to-moderate earthquakes ($0 \le M_L \le 4.5$) recorded between 2016 and 2025 to image lateral variations in crustal stress using the Energy Index (EI), a moment-energy parameter sensitive to rupture efficiency. By extending the RAMONES framework to this region, we detect pronounced east–west contrasts in fault mechanical behavior: high EI values in the west mark zones of reduced frictional strength, whereas low EI in the east suggests mechanically stronger, segmented fault domains. These spatial patterns align with independent geophysical indicators (V_P/V_S, Q_P), indicating a strong link between mechanical segmentation, material properties, and permeability structure. Our results demonstrate that small earthquakes carry diagnostic signatures of fault-zone strength and segmentation, providing a scalable tool to resolve stress heterogeneity and refine seismic hazard models in structurally complex regions.

Understanding fault strength is a key objective in seismology, as many unresolved scientific questions, such as how faults interact and how large earthquakes initiate, ultimately relate to the mechanical properties of faults and the surrounding crust. Studying only large earthquakes is insufficient to grasp in situ crustal strength, because they are infrequent and primarily reflect the transient phase of the rupture process. Seeber and Armbruster (2000)[1] suggested using minor and micro-earthquakes as proxies for the mechanical state of the crust by analyzing their static Coulomb stress changes. Minor earthquakes poorly interact with each other due to their small size[2] and contribute minimally to crustal deformation. However, they are highly sensitive to variations in stress conditions. Thanks to the efforts of the seismological community in deploying dense seismic networks in earthquake-prone regions, standardizing data transmission and archival formats, and establishing open-access repositories for real-time and historical data, it is now possible to explore such principles by studying tiny earthquake rich datasets to reveal fault strength variations and mechanical segmentation (Brodsky, 2019)[3]. In recent years, several studies have investigated the spatial variability of minor earthquake source parameters, particularly stress drop ($\Delta\sigma$) to identify and analyze fault segmentation[4–13]. These studies collectively demonstrate how analyzing spatial variations in earthquake source parameters can reveal structural and mechanical differences along fault systems. This information has significant implications for seismic hazard assessment.

The Adriatic Indenter in the European Eastern Alps is a complex seismotectonic region resulting from the interaction between the Eurasian plate and the Adriatic microplate[14–16]. Here, the whole set of tectonic styles coexists (i.e., compressive faults, strike-slip systems and, to a small extent, extensional structures), and associated to them a long record of moderate to strong seismicity exists, which includes the '1117 Verona Earthquake' (Me 6.8) in the Venetian plain[17], the '1348 Villach Earthquake' (Me 6.6) near the border between Italy, Slovenia and Austria[18], the '1695 Asolo Earthquake' (M_w 6.5) along the southernmost alpine fronts[19], the '1511 Idrija Earthquake' (M_w ~6.8) linked to the Dinaric strike-slip fault system[20], and the more recent '1976 Friuli Earthquake' (M_w 6.5) which was caused by thrust faulting along the southern Alps front[21]. Geodetic and seismological studies in the southeastern Alps (NE Italy) reveal persistent crustal shortening and strain

[1]National Institute of Oceanography and Applied Geophysics – OGS, Trieste, Italy. [2]Servizio Geologico, Provincia autonoma di Trento, Trento, Italy. [3]DISTAV, University of Genoa, Genoa, Italy. [4]Helmholtz Centre Potsdam, GFZ German Research Centre for Geosciences, Potsdam, Germany. [5]University of Naples Federico II, Naples, Italy. ✉email: mpicozzi@ogs.it

accumulation at rates of ~ 2–10 × 10^{-8} yr^{-1}, placing the region among the most actively deforming continental intraplate zones in Central Europe[22].

Seismicity in the study area is monitored through coordinated Italian and international networks, operating in close cooperation with neighboring countries (see Data Availability and Resources). To better understand the seismotectonic framework of the southeastern Alps, we reprocessed seismicity in the period 2016–2025, and we analyzed 9,249 earthquakes with magnitude in the range $0 \le M_L \le 4.5$ recorded by permanent seismic networks (Fig. 1, see Data and Resources). We implemented the Rapid Assessment of Seismic Moment and Radiated Energy in Central Italy (RAMONES) procedure[23] for the European Eastern Alps region. We significantly expand the set of available earthquakes with respect to previous studies for this region[24–30]. In the wake of the McGarr's[31] original claim that seismic moment (M_0) and radiated seismic energy (E_S) provide valuable information about the state of the crustal stress and how it evolves toward failure, we investigate their spatial and temporal distribution. Combining M_0 and E_S provides a different perspective on the dynamic of seismic ruptures (i.e., M_0 is a static measure of the earthquake size and E_S is related to the kinematics and dynamics of the rupture[10,32–36].

Brown and Hudyma[37] proposed to exploit the parameter Energy Index (EI), defined for each earthquake as the difference of logarithms between the observed E_S and the prediction from the reference $E_S - M_0$ model, as an indicator of the stress around mining sites. Picozzi et al.[8,36,38] examined the evolution of EI over time and space in southern Italy, as well as in the lead-up to the large earthquakes that have occurred in central Italy since 2009. These studies showed that EI revealed signs of preparation processes before the large earthquakes, particularly the 2009 L'Aquila. The EI analysis also identified areas of high stress around which the M_w 6.2 Amatrice and M_w 6.5 Norcia earthquakes have nucleated. The EI analysis can be applied regardless of the method used to estimate E_S and M_0. The advantage in using the RAMONES approach is that we derive E_S and M_0 by measuring specific ground motion features directly on seismograms (i.e., the S-wave peak ground displacement, PD_S, and the integral of the squared velocity, $IV2_S$) and correcting them for propagation and site effects using empirical models calibrated for the region of interest. The main advantage of our approach is that it resembles algorithms for magnitude computation, and is therefore suitable for monitoring purposes in rapid response frameworks.

By studying the EI distribution in the southeastern Alps region, we confirm and extend the results of previous studies. Our findings highlight significant differences in the mechanical properties of fault systems in the eastern and western sectors of the investigated area. Building on these insights, our study enhances the seismotectonic understanding of the region by analyzing the source parameters of small earthquakes in detail It also lays the groundwork for integrating advanced source-related metrics, such as the Energy Index, into operational seismic monitoring frameworks. This integration can improve the characterization of faults in real-time and the early detection of seismic precursors. Ultimately, it contributes to more effective seismic hazard assessment and mitigation strategies in complex tectonic regions. By leveraging the Energy Index and the detailed analysis of small-magnitude earthquakes, we introduce a paradigm shift in fault system studies and seismic monitoring, where detecting spatial and temporal anomalies in source parameters becomes key to identifying preparatory phases of large earthquakes.

Results

Energy index Estimation

We derive the backbone scaling model relating $\log(M_0)$ and $\log(E_S)$ for 9,249 earthquakes (Fig. 2a) and we compute the Energy Index, EI, as the difference between the experimental E_S estimates (E_{Sobs}) and the predictions from the reference $E_S - M_0$ model (E_{Spr}, Eq. 3), where the input is the seismic moment M_0 from recorded earthquakes (see Methods). Positive (and negative) EI values indicate events radiating more (less) energy per unit-slip and unit-area (i.e., M_0) than the average in this region (Eq. 3). EI presents neither temporal variations (Fig. 2b) nor any trend with respect to M_w or hypocentral depth (Fig. 2c). The EI distribution is symmetric with a zero mean (Fig. 2d).

The estimates of seismic moment, M_0, are used to compute the moment magnitude[39,40], M_w. The latter is, in turn, used to study the frequency magnitude distribution for the earthquakes at hand. We estimate the completeness of magnitude[41,42], Mc, which results equal to 1.1 +/- 0.3, and the b-value (i.e., the slope of the Gutenberg–Richter[43] frequency–magnitude relationship) by applying the maximum likelihood approach[44] and assessing the uncertainty by a bootstrap approach[45]. The b-value estimate is equal to 0.97 +/- 0.02 (Fig. 2e). Therefore, for investigating the spatial distribution of EI, we select earthquakes with magnitude $M_w \ge 1$ and hypocentral depths between 2.5 km and 15 km (Fig. 2f), which encompasses the seismogenic volume where large earthquakes are generated, for a total of 4338 earthquakes.

EI space-time analysis

When we map the selected earthquakes colored per EI, we can observe already at first glance, a marked spatial trend for the investigated area (Fig. 3a). Keeping as threshold the Longitude 12°, we observe a dominance of positive EI values (EI > 0, hereinafter EI+) in the western sector and of negative (EI < 0, hereinafter EI-) and moderately positive ones in the eastern sector. We show the EI map without the selection in magnitude in Figure S1. To map the spatial variability of EI, we also create a regular three-dimensional grid of size 10 km. For each grid node, we select all the events within a maximum distance from the node equal to the grid size, as described in Picozzi et al. (2021)[46]. Nodes with less than five earthquakes are discarded. The uncertainty associated with EI is estimated following a bootstrap approach[45] and repeating the computation of EI images with 100 random sampling realizations of the original data set with replacement. We then compute the mean of EI, $\langle EI \rangle$, and the standard error considering the 100-bootstrap realization. The $\langle EI \rangle$ map (Fig. 3b) confirms the east-west trend in energy radiation, while the uncertainty is very small (Figure S2).

To investigate the spatial variability of EI, we apply the density-based clustering DBSCAN[47]. The purpose of this clustering is not to define the main longitudinal fault segmentation itself, which is primarily inferred

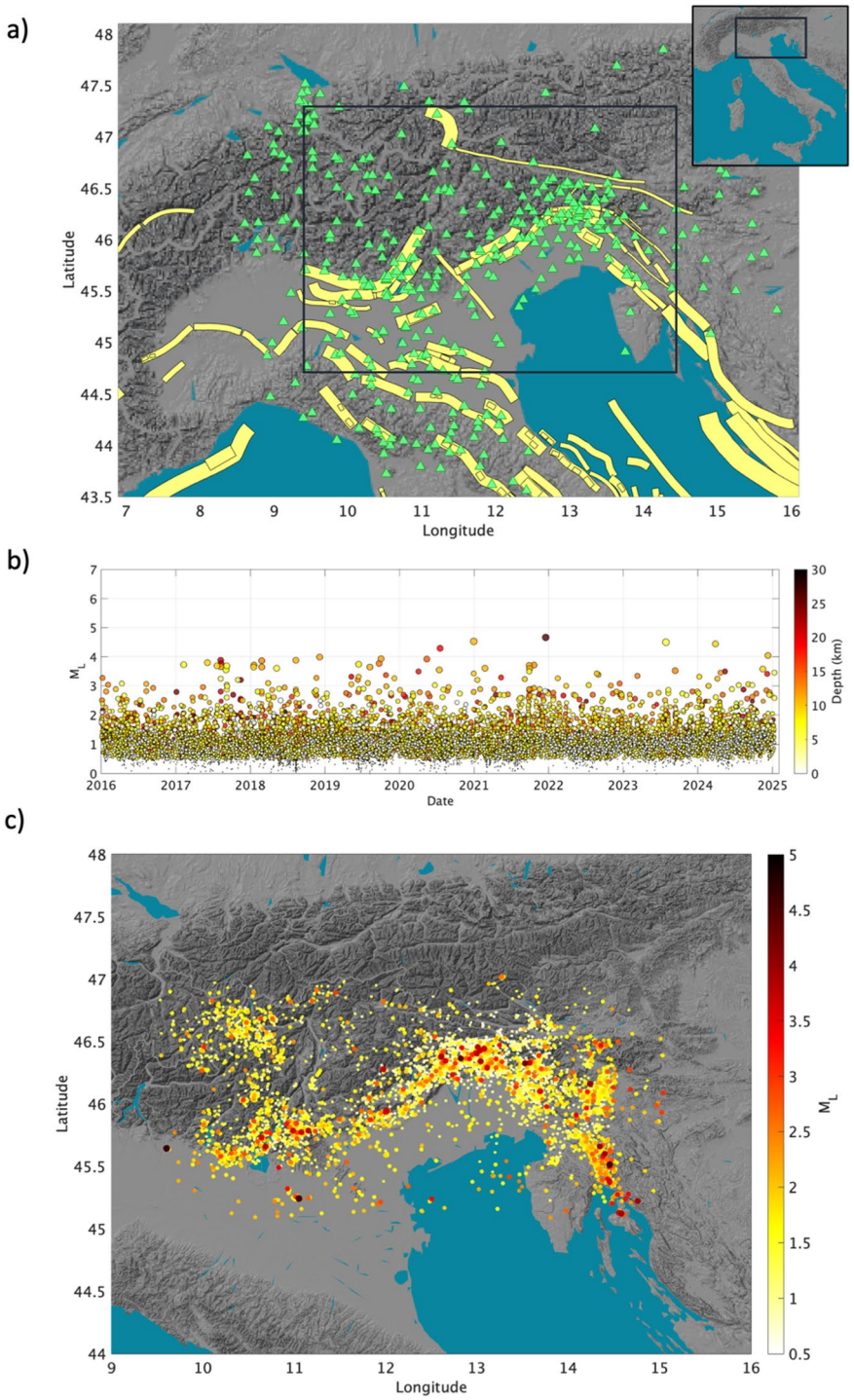

Fig. 1. **a**) Map showing the seismic stations (green triangles; see section "Data availability and resources" for the DOI associated to each network) and the seismogenic sources from DISS (https://diss.ingv.it).**b**) Temporal evolution of seismicity considering the local magnitude, M_L and with data colored per hypocentral depth. **c**) Map showing the spatial distribution of earthquakes colored per M_L. The maps were done using Matlab software R2022b, https://it.mathworks.com/, last accessed December 2025.

from the along-strike energy patterns. Rather, it supports identifying internally consistent groups of events in the space-energy domain. Clustering is performed using normalized hypocentral coordinates together with the EI parameter. Specifically, the spatial coordinates are linearly normalized to the [0,1] interval so that spatial information and EI have comparable magnitudes and no single parameter dominates the distance metric used in the clustering algorithm. After some tuning of the algorithm parameters (setting the neighborhood distance around a given point ε to 0.1 and the minimum number of points in a neighborhood Z to 19) and considering

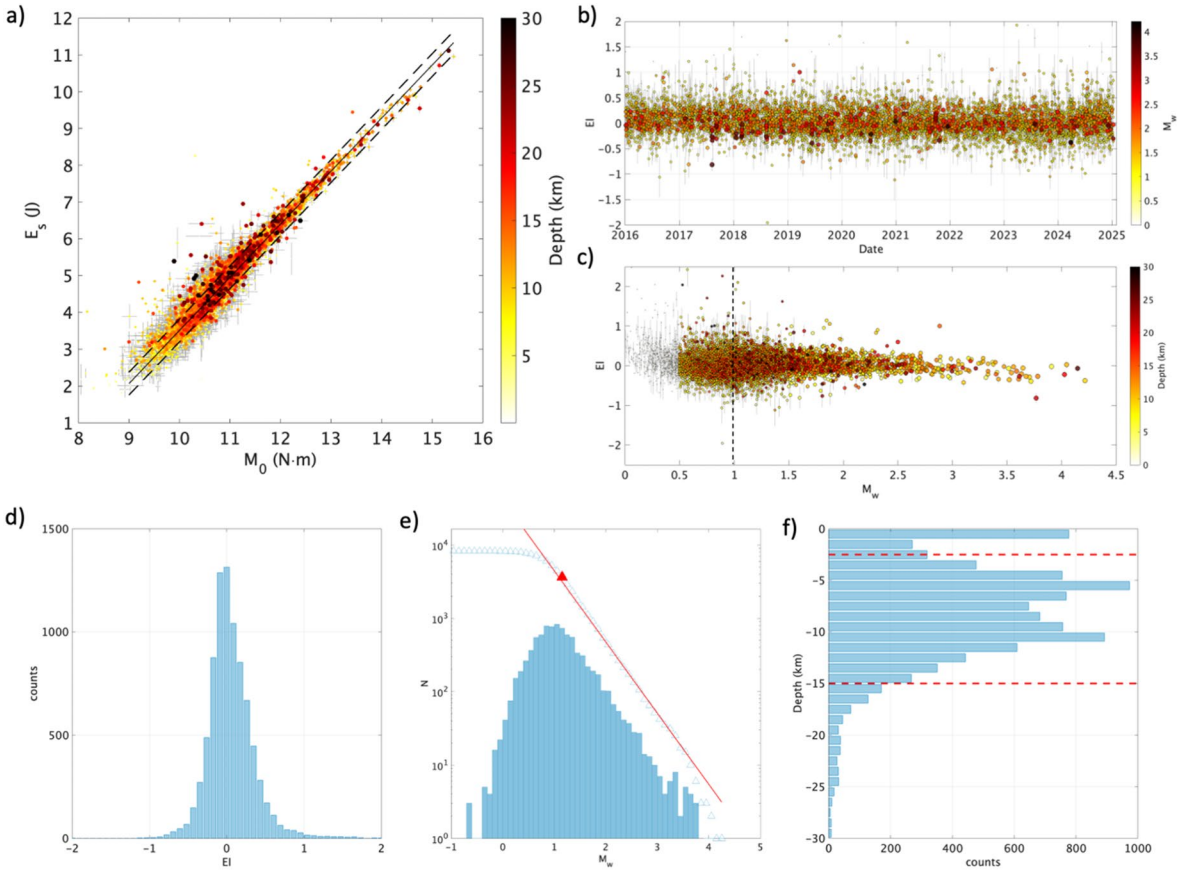

Fig. 2. **a**) E_S versus M_0 with data colored per hypocentral depth. Backbone scaling model (Eq. 3; black line) and +/- 1 standard deviation (black dashed lines). **b**) EI in time with data colored per M_w. **c**) EI versus M_w with data colored per hypocentral depth and size per M_w. Threshold magnitude equal to M_w 1 (black dashed line). **d**) distribution of EI. **e**) Frequency magnitude distribution of M_w. The parameterization of the Gutenberg–Richter relation is reported within the plot (red line). Mc is represented as a red triangle. f) distribution of hypocentral depths. Thresholds in hypocentral depth used for data selection (red dashed lines).

the normalized earthquake coordinates and EI as input parameters, we observe in Figures (3c and 3d) the seismicity being classified in four clusters (i.e., IDs from 1 to 4), plus one undefined class of events (i.e., ID 5, with 1673 events). Clusters 1 and 2 (with 1702 and 150 earthquakes, respectively) are similar to each other, as those of clusters 3 and 4 (with 301 and 512 events, respectively). Overall, the cluster analysis also confirms the spatial variability of EI and the different radiation capabilities of small earthquakes in the eastern and western sectors.

To better understand the EI spatial distribution, we consider equal bins in Longitude (i.e., each bin 0.25 degrees wide) and we count the positive and negative EI values (i.e., EI + and EI-, respectively). Thus, we observe (Figure S3a and b) that the number of EI + and EI- is comparable in the eastern sector, while the number of EI- is strongly reduced for Longitudes smaller than 12°. Figure (S3c) clarifies better the proportion of events in the two classes as the percentage of EI- values with respect to the total data. More in detail, EI + values appear to be distributed over the whole Longitude range, even if those in the western sector have larger EI than those in the eastern one. Moreover, the population of EI + might be further divided into three sub-groups of events separated by gaps at Longitude 11.5° and 14°. Even the EI- distribution shows a gap at Longitude 14° (Figure S3b), but here the striking feature is the significant drop of all the events for longitudes smaller than 12°. The different spatial-temporal distribution of events can be appreciated by representing those with EI + and EI- separately (Figure S4).

If we consider the threshold Longitude 12° to divide the dataset in two families, we can confirm that the resulting EI distributions present different amounts of data and medians (Figures S5a and S5b). The population of earthquakes in the eastern sector is larger and has a median slightly lower than zero, while those in the western sector are characterized by a positive median. To verify if these spatial differences in the EI distribution are related to the network characteristics and different detection capabilities between the eastern and western sectors, we analyze the frequency-magnitude distribution, FMD, for the events belonging to the two areas. Figure (S5c) shows that, despite the different number of events, the eastern and western populations look very similar, and that considering the uncertainties they appear characterized by the same magnitude of completeness, Mc ~ 1 and b-value ~ 1. Therefore, we can reasonably conclude that the EI differences observed between the two sectors are not related to different performance of the monitoring network for the two areas.

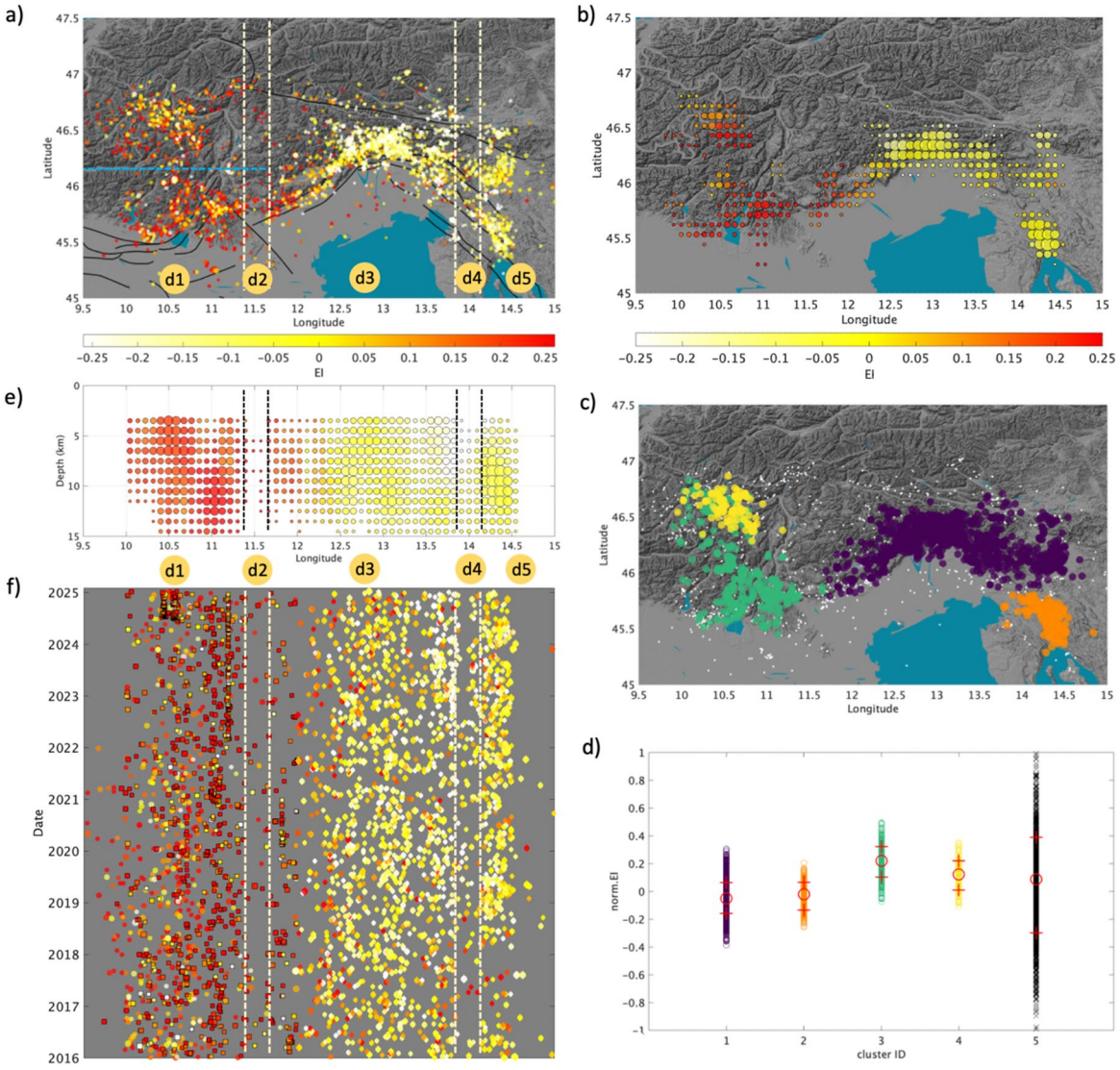

Fig. 3. **a**) Distribution of earthquakes colored per EI. Seismogenic sources from DISS (https://diss.ingv.it; black lines). White dashed lines identify the five domains discussed within the text. The light blue dashed line separates EOA and CSA_MG faults (see text). **b**) Map showing the mean of EI, $\langle EI \rangle$, over a regular grid. The dimension of dots is related to the amount of data for grid node. **c**) Clusters from DBSCAN, data are colored per cluster ID as in panel d), with the exception of cluster ID-5 for which data are white dots. **d**) Cluster families. For each of them, the median (red circle) and +/- 1 standard deviation (red crosses) are reported. **e**) Obtained using the same gridding strategy of **b**), but distribution of $\langle EI \rangle$ for a cross section along Longitude direction with 1 km spacing in depth. **f**) Spatio-temporal distribution of EI. The maps were done using Matlab software R2022b, hthttps://it.mathworks.com/, last accessed December 2025.

As an additional check, we verify whether the spatial distribution of the EI changes with the depth of the events. We divide the dataset in two families: shallow events with hypocentral depth in the range 2.5 km to 7.5 km (Figure S6a); deeper events with hypocentral depth in the range 7.5 km to 15 km (Figure S6b). Despite the presence of a few minor differences, we observe for both cases the same general spatial trend with larger EI values in the western sector. The ⟨I⟩ maps (Figures S6c and S6d, while the associated standard error maps are shown in Figures S6e and S6f) confirm the main east-west differentiation in EI distribution, so as even when we split our dataset into larger ($M_w > 2.5$) and smaller ($1 \leq M_w \leq 2.5$) earthquakes (Figure S7). All these tests confirm that the observed spatial distribution of EI is, to first order, free from effects of the hypocentral depth and magnitude.

The pronounced east–west contrast in faults seismic radiation potential appears even clearer when we plot the distribution of EI with depth (Fig. 3e) and its spatio-temporal distribution (Fig. 3f). We do not observe significant temporal variations in EI. Thus, we can assume that our results provide a picture of what the state of the faults has been over the past 10 years.

Discussion

Spatial variations in EI could be linked to various factors (e.g., tectonic stress, frictional properties, nucleation length or propagation speed of the rupture). Since the b-value is similar in the western and eastern sectors (Figure S5c), we assume that the tectonic stress is similar throughout the region under study. Since currently we have no evidence of variation in nucleation length or rupture propagation speed, we interpret the spatial variations in EI as a proxy for variations in frictional stress, σ_f.

Following Kanamori and Heaton (2000)[48] and Zuñiga et al. (2025)[49], we relate the Energy Index with a simplified outline of the rupture process (Fig. 4). We assume the Orowan's model[50] (i.e., when the final stress equals the frictional stress) as the condition of events with radiated energy in agreement with the energy-to-seismic moment backbone scaling model (i.e., earthquakes with EI equal zero, Fig. 4a). Cases in which the frictional stress averaged over the fault surface is higher than the final stress are identified as 'frictional overshoot'. In the case of overshoot, the total radiated energy is less than that in the Orowan case (i.e., comparison between Fig. 4a and b), and the dynamic stress drop averaged over the rupture surface, $?\sigma_d?$, is lower than in the Orowan case (i.e., the average dynamic stress drop is defined as the difference between the initial stress and the frictional stress). Therefore, we can interpret negative EI values as indicative of overshoot rupture processes. Finally, when the final stress exceeds the average frictional stress, the rupture process is described as 'partial stress drop' or 'undershoot', which corresponds to an excess of radiated energy with respect to the Orowan's model (i.e., Figs. 4c versus 4a, positive EI in our case). In these cases, $?\sigma_d?$ is high. We show in Figure (4d) the susceptibility to develop ruptures under high or low σ_f, by considering EI > 0.015 related to low σ_f, and EI < -0.015 for high σ_f. To focus our discussion also on structures, we consider the seismogenic sources from DISS (Database of Individual Seismogenic Sources; https://diss.ingv.it, DISS Working Group, 2021[51]) and we classify them in terms of σ_f considering the average of the EI values for the earthquakes included within each source area. Sources with less than ten EI values within their area are discarded.

We can exploit this conceptual framework, where EI is assumed as a proxy of σ_f, and the pieces of information from previous studies, to interpret the fault-zone strength and segmentation in the investigated area. In particular, we refer to the simplified seismotectonic domains[22] (Figure S8), the results in terms of stress drop and seismic efficiency obtained by Cataldi et al. (2025)[30], the velocity and attenuation tomographic study from Jozi Najafabadi et al. (2023)[52] and the geodetic study from Cheloni et al. (2014)[53] and Serpelloni et al. (2016)[54]. Moreover, we include into our analysis the moment rate estimation ($\dot{M}_0$), which is computed for equally spaced longitude bins, each 0.25 degrees wide (see Methods). For a more detailed analysis of the areas, we also suggest Viganò et al.[15,55] and Bressan et al. (2012)[56].

The joint perspective of EI spatial distribution, $\dot{M}_0$ and the distribution of historical large earthquakes[57] illustrates a Southeastern Alps faults system with spatially varying properties (Fig. 5). Hence, we tentatively defined a few spatial domains with homogeneous characteristics (Figs. 3a, e, f), and we sketched their main properties.

Domain d1

Following Villani et al. (2024)[22], the western domain (i.e., the area with longitude smaller than 11.5°, hereinafter d1) includes the Engandine-Ortles Alps (EOA), the Central-Southern Alps and Meran-Giudicarie (CSA-MG), the Brenner-Jaufen Oetzal (BJO), and the Schio-Vicenza-Lessini (SVL) termination. Seismicity in d1 appears diffuse and stationary over time, and is characterized by high EI. It is worth noting that Cataldi et al. (2025)[30] observed that this area is markedly populated by earthquakes with high efficiency. Two sub-domains can be identified therein (separated by the Periadriatic Lineament and with completely different tectonic histories): the first belongs to the internal Alpine chain, the second to the Giudicarie system. These subdomains are also separated by an area of reduced seismicity in a narrow sector around latitude 46.2° (light blue dashed line in Fig. 3a). Furthermore, Jozi Najafabadi et al. (2023)[52] found higher P-waves attenuation (low Q_P) in EOA than in CSA_MG, as well as different P-wave over S-wave velocity ratios (V_P/V_S) between the two areas (i.e., higher V_P/V_S in CSA_MG and lower values in EOA). These findings support the differentiation of d1 into two sub-domains. Moderate to high V_P/V_S values in the southern Giudicarie sector (Southern Giudicarie and Lake Garda areas) were also obtained at a more detailed spatial scale[55].

Overall, d1 is characterized by high seismic efficiency, variable V_P/V_S values (higher in the southern subdomain and lower in the northern one), medium-to-low Q_P, and a moment rate that increases from west to east (Fig. 5). The increase in seismic moment rate ($\dot{M}_0$) suggests that deformation on the eastern side of the domain is being released efficiently through seismic slip.

We inferred low frictional stress from EI, which suggests the presence of mechanically weak faults. Once initiated, the rupture can propagate efficiently, causing stronger shaking. The medium-to-low Q_P may reflect localized crustal damage, which is consistent with the structural complexity of the Trentino region. Crustal fluids could then concentrate on the localized fault damage zones, playing a critical role in promoting large earthquakes. However, d1 has historically experienced a reduced number of large earthquakes compared to other domains further east. Within d1, DISS faults interpreted with low σ_f are AP, WSA, MB, G and SVL (Table S1). Future studies of this domain should verify whether these faults are highly sensitive to stress perturbations and can easily reactivate, especially under modest stress transients (e.g., hydrological, anthropogenic, or afterslip loading) as previously suggested[58].

Domain d2

Figure (3) shows that as one moves east from d1, the seismicity and $\dot{M}_0$ decrease, though sporadic earthquakes remain characterized by a high EI. The second spatial domain (d2) roughly corresponds to the western sector of the Southeastern Alps (SEAW) and the southern portion of the Schio-Vicenza-Lessini (SVL). Geodetic studies[53,54] identified the thrust front through the analysis of geodetic and seismological data as a sector

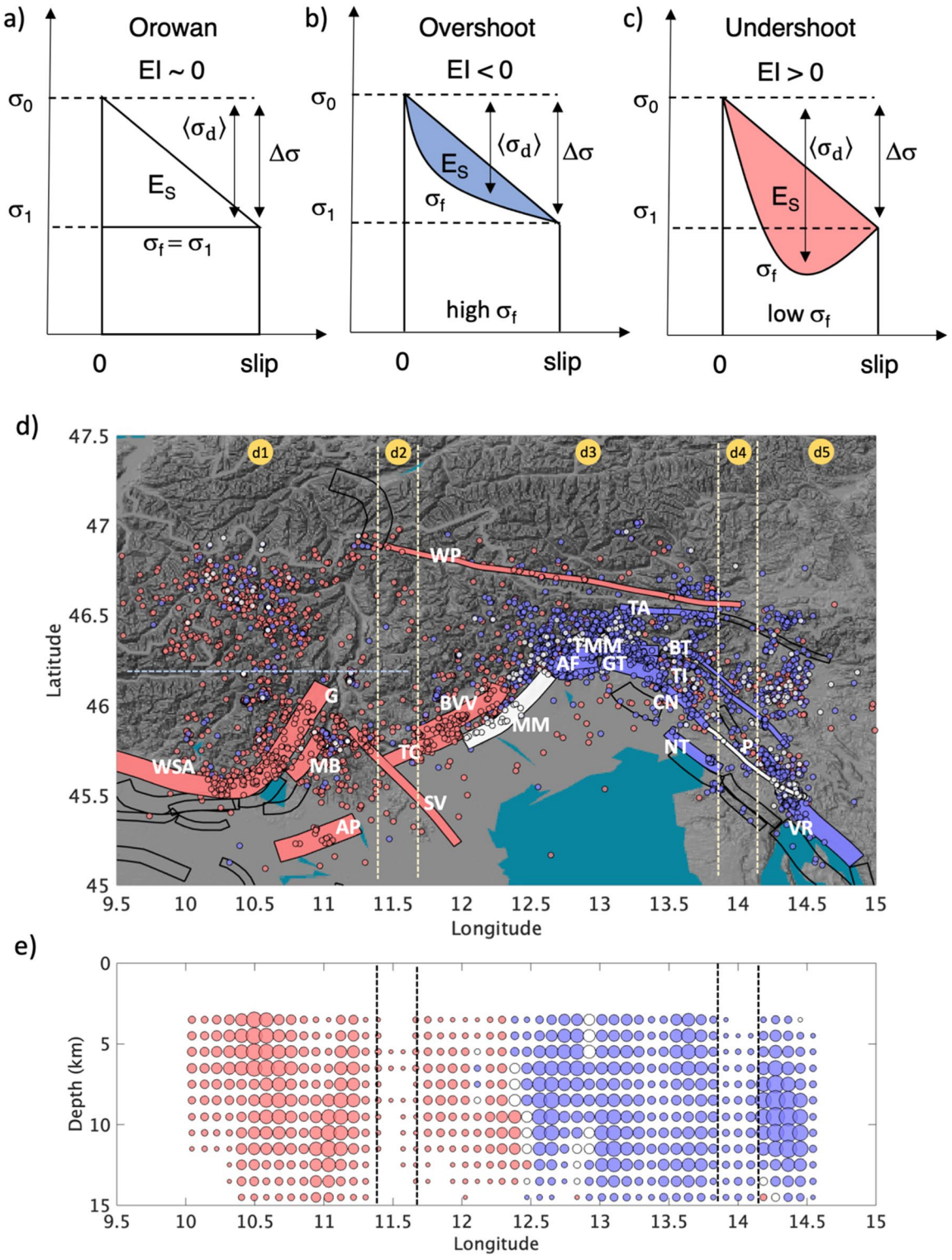

Fig. 4. Models illustrating the relationship between the stress levels and the radiated seismic energy for a simplified earthquake faulting. **a**) Orowan model. **b**) Model with higher frictional stress with respect to Orowan model. **c**) Model with lower frictional stress with respect to Orowan model. **d**) Spatial distribution of earthquakes colored according to EI values and the outline of a simplified earthquake faulting shown in subplots **a**) to **c**) (The map was done using Matlab software R2022b, https://it.mathworks.com/, last accessed December 2025). Seismogenic sources from DISS (https://diss.ingv.it; see Table S1 for the faults code) colored as the mean of the earthquakes EI when their area includes more than ten events. **e**) but distribution of $\langle EI \rangle$ colored according to the outline of a simplified earthquake faulting shown in subplots **a**) to **c**) plotted for a cross section along Longitude direction. The dimension of dots is related to the amount of data for grid node.

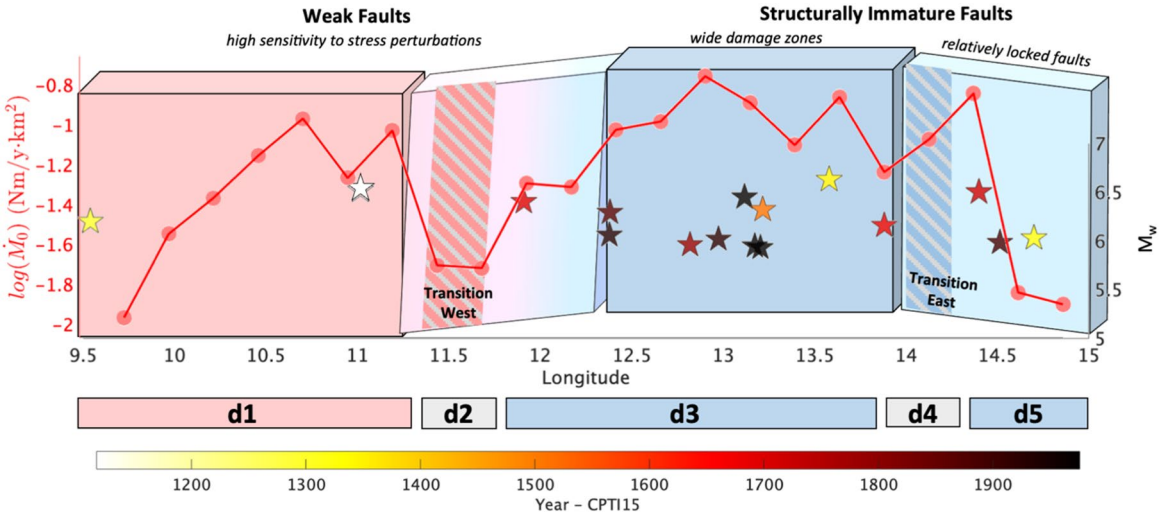

Fig. 5. Outline summarizing the unified observations. Southeastern Alps is sketched in blocks plotted for a cross section along Longitude direction and colored according to the outline of a simplified earthquake faulting shown in Fig. 4. The logarithm of moment rate is shown in red. The magnitude of historical seismicity (all events with magnitude above 5.5 in the time range 1000–2020, taken from the Italian Parametric Earthquake Catalogue, CPTI15[57]) is shown along the Longitude direction and colored per year of occurrence. The magnitude axis is represented on the right side of the plot.

with reduced coupling. Very high Q_P (i.e., low attenuation) and low V_P/V_S were found for this domain[52,55]. Jozi Najafabadi et al. (2023)[52] hypothesize that this anomaly in attenuation and velocity ratio is a southern prolongation of the Dolomites Indenter (DI). There, the observed medium properties are associated with stiff Permian magmatic rocks. Alternatively, it could be a specific feature of this sector of frontal thrusts, between the SVL strike-slip system to the west and active the strike-slip faults (as evidenced by the M_w 6.5, 1695 Asolo earthquake) to the east, i.e., the Montebelluna (MB) fault. According to Viganò et al. (2015)[15] seismotectonic model, this area was interpreted as subject to strain partitioning along dominant strike-slip faults.

A sector with very low seismic moment rate relative to its neighbours as d2 is not simply quiet, rather mechanically different. d2 may be a potentially locked fault segment that has accumulated elastic strain, increasing the risk of a future moderate-to-large earthquake. Alternatively, in agreement with previous observations, part of the deformation in d2 may be accommodated aseismically. Future targeted high-resolution multi-parameter monitoring (e.g., InSAR, GNSS, fluid geochemistry, and microseismicity) would help distinguish between locked and creeping behaviors.

Domain d3

Going further east, we find a wide domain (d3) marked by abundant seismicity but moderate to low EI (Fig. 3a) but high $\dot{M}_0$ (Fig. 5). This domain encompasses both the western and eastern sectors of the Southeastern Alps (SEAW and SEAE, respectively), the External Southeastern Alps (ESEA) and the Dinarides (DIN) (Figure S8). According to Jozi Najafabadi et al. (2023)[52], d3 is characterized by high attenuation (low Q_P), high V_P/V_S, and high coupling[53,54]. The high V_P/V_S are also confirmed for the westernmost sector of d3 by Viganò et al.[15,55]. Worth to note d3 is the domain with the highest strain rate of the entire analyzed area, and Bressan et al. (2012)[56] found in the M_w 6.5, 1976 Friuli earthquake epicentral area a high-stiffness rock volume between 4 km and 8 km of depth. Earthquakes with low relative stress drop were found here[30] (i.e., earthquakes with an experimental stress drop smaller than the theoretical stress drop calculated for the same seismic moment and using a best-fitting model obtained from the distribution of source parameters).

The high frictional stress of the DISS faults identified in d3 (i.e., AF, CN, GT, TA, TI, TMM, and BT) combined with a high moment rate (Fig. 5) suggests that these faults are structurally immature (i.e., with limited cumulative slip).

The high V_P/V_S ratio and low Q_P suggest the presence of fluids, especially in the liquid phase, in a fractured and heterogeneous crustal medium, with damage zones that attenuate seismic waves. The abundant diffuse seismicity indicates that earthquakes are not confined to a single major fault, but rather distributed across a network of secondary structures. This is consistent with the release of the accumulating stress through moderate swarms or sequences[59]. Nevertheless, this region has a high seismic hazard, and its seismogenic structures are capable of generating moderate to large earthquakes, such as the 1511 Idrija and 1976 Friuli earthquakes (Fig. 5). To study the seismic and deformation behavior in this region, the OGS (National Institute of Oceanography and Applied Geophysics) and the University of Trieste recently proposed the creation of the North-Eastern Thrust Faults Observatory (NITRO) as part of the European Near Fault Observatory (NFO) network (https://www.epos-eu.org/tcs/near-fault-observatories)[60].

Domain d4

We identify a domain of reduced seismicity east of d3 and within the Dinarides area (DIN). Unlike d2, this narrow fourth domain (d4) has small to moderate EI. In contrast to d3, Jozi Najafabadi et al. (2023)[52] observed a progressive increase in Q_P here, though V_P/V_S remains high Domains with reduced seismicity obviously attract attention because there are two possible scenarios (i.e., a seismic gap versus creeping faults) with opposite implications for seismic hazard. As for d3, the friction properties in this domain may result from the roughness and geometry of the fault. Reduced seismicity (Fig. 4) suggests that locked faults or asperities are resisting rupture and accumulating elastic strain. The high V_P/V_S suggests the presence of fluids, though not enough to significantly reduce friction. Therefore, fluids might possibly be confined to areas outside the fault core. Taken together, these observations suggest that d4 merits further investigation for possible insights into the preparatory phases of large earthquakes.

Domain d5

Finally, we identify a fifth domain (d5), in which the seismicity appears to be organized into two main clusters. The northern cluster belongs to the Southeastern Alps (eastern sector, SEAE), and the southern cluster belongs to the Dinarides (DIN). Unfortunately, d5 falls outside the well-resolved area for the attenuation and tomographic images[52], and it is also outside the area analysed with geodetic data[53,54]. Cataldi et al. (2025)[30] observed in d5 events characterized by low efficiency in the SEAE/DIN convergence zone and high efficiency in the DIN region. We observe $\dot{M}_0$ progressively decreasing towards east. Our results, combined with the past occurrence of a few large earthquakes, suggest the presence of relatively locked faults requiring high stress accumulation to rupture (Fig. 5). The low seismic efficiency in case of small earthquakes in the SEAE/DIN convergence zone implies that much of the accumulated tectonic energy is not released as seismic waves, but is likely dissipated via frictional heating and off-fault deformation. Low seismic efficiency may also suggest complex fault geometry, which inhibits dynamic rupture propagation. Clustered seismicity suggests localized zones of stress concentration, possibly near structural barriers or fault bends. These observations are consistent with the complex tectonic framework of this region that marks a transitional zone between the Southern Alps and the External Dinarides, with complex thrust and strike-slip interactions.

In conclusion, the spatial distribution of the Energy Index (EI), which is derived from the analysis of small earthquake source properties, highlights the first-order segmentation of the faults system. This has improved our understanding of the tectonics of the European Eastern Alps. This study provides information that can be useful for the seismic hazard assessment. Incorporating the spatial and temporal patterns of minor seismicity into fault characterization frameworks improves our ability to model seismic potential and develop targeted monitoring strategies. This approach is particularly important for regions such as the European Eastern Alps, where multiple fault systems interact across variable rheological and structural domains.

Future developments will include estimating EI (i.e., the estimation of seismic moment and radiation energy for small-magnitude earthquakes) for the European Eastern Alps as part of a monitoring service for routine operations, similar to the RAMONES service for central Italy[23]. Monitoring EI over time for the European Eastern Alps may offer insights into the preparatory processes of large-magnitude earthquakes, as has been observed retrospectively for the 2009 L'Aquila earthquake[38]. Additionally, we will also exploit the small-magnitude earthquakes in the area to study the static friction coefficient along the faults[61].

Our study, together with previous findings from the analysis of the Central Italy seismic sequences, suggest that the time is now ripe to apply advanced research methodologies to operational seismic monitoring. Specifically, years of investigations on microseismicity (focused on seismic moment, radiated energy, and ground motion parameters) enable us to systematically integrate additional source-related information into real-time monitoring workflows. Along with standard location and local magnitude (M_L) estimates, we advocate for the routine computation of anomalies with respect to empirical reference models, such as the Energy Index (EI). The EI provides valuable insights into fault frictional properties and stress conditions. Leveraging the EI and the detailed analyses of small-magnitude earthquakes introduces a paradigm shift in fault system studies and seismic monitoring. Detecting spatial and temporal anomalies in source parameters can be a key strategy for identifying preparatory phases of large earthquakes[62–64]. The first operational step was to implement the estimation of EI for Central Italy through the RAMONES service[23]. This service provides a routine, though not real-time, computation of seismic moment and radiated energy. The next logical step is to transfer and integrate this methodology into the official seismic monitoring and surveillance system for Northeastern Italy, which is managed by the Centro di Ricerche Sismologiche (CRS) of OGS in Udine. This integration will enhance real-time capabilities by incorporating advanced source parameters, thereby supporting more effective fault characterization and the timely recognition of potentially critical seismic patterns.

Data

We consider an initial pool of 13,568 earthquakes available from the OGS bulletin (https://www.crs.inogs.it/bollettino_new/; see section Data availability and resources and supplemental material), occurred in the period 2016.01.01–2025.01.10, and recorded by 445 velocimetric and accelerometric stations from the seismic networks monitoring the area (Fig. 1), both permanent and temporary (a list of used stations is available in the Electronic Supplements, while DOIs and additional information are reported in the Data Availability and Resources section).

Concerning the preprocessing, we followed Spallarossa et al. (2021)[23] and we implemented: the instrumental correction and automated picks using the procedure[65]; the event re-location using the NonLinLoc software[66]; the estimation of the local magnitude M_L by averaging the station magnitude estimates and considering the zero-magnitude attenuation model calibrated by Di Bona (2016)[67] for Italy, but without applying station corrections, to have homogeneous estimates of the magnitude size for all events.

The location was carried out using the 1D regional velocity model[68] as in the OGS localizations and Cataldi et al. (2025)[30]. The locations are thus in agreement with those of the OGS bulletin, with uncertainties in event locations mostly within 1 km horizontally (Erh) and 2 km vertically (Erz) (Figure S9).

We then select a subset of 9,249 earthquakes (Fig. 1) with magnitude in the range $0 \le M_L \le 4.5$ that satisfies the following quality criteria: events localized using at least 12 phases; events with Erh ≤ 3 km and Erz ≤ 5 km; events with azimuthal gap less than 200° (Figure S1).

Methods

Energy index

Our methodology is implemented in two steps and follows Picozzi et al.[33,36] and Spallarossa et al. (2021)[23].

Step 1. Calibration of empirical Attenuation models for source parameter proxies

Here, we summarize the RAMONES processing workflow.

We consider the source parameters M_0 and E_S of 681 earthquakes from Cataldi et al. (2025)[30] and we analyze their waveforms to estimate, for each recording, the S-wave peak displacement (PD_S) and the integral of the squared velocity ($IV2_S$) over the S-wave window. These earthquakes are distributed over the whole region of interest (Figure S10a), the hypocentral depths are mostly included between 5 km and 15 km (Figure S10b), and the magnitudes cover the range M_w 1.5 to M_w 4 (Figure S10c).

Following the procedure developed by Scafidi et al. (2019)[65], a high-pass corner frequency of the pre-deconvolution filter is automatically determined based on signal-to-noise analysis, selecting the lowest frequency in the 0.3–2.0 Hz range for which the signal-to-noise ratio is larger than 4.0.

We compute the PD_S and $IV2_S$ considering a time window starting 0.1 s before the S-wave onset and ending at different percentages of the cumulated energy varying with the source to site distance R: (i) 90% when $R < 25$ km; (ii) 80% when 25 km $< R <$ 50 km; (iii) 70% when $R > 50$ km. We imposed a minimum time window length of 2.5 s and a maximum time window length of 20 s for both PD_S and $IV2_S$. For each recording, we measure the signal-to-noise ratio considering a pre-event noise window of the same length as the direct S-waves. For PD_S the estimates from the NS and EW components are averaged (geometric mean), while for $IV2_S$ the estimates for three components of ground motion are summed up.

The PD_S and $IV2_S$ values relevant to the *k*th earthquake recorded at the *l*th station are then linked to M_0 and E_S, respectively, through the following empirical attenuation models:

$$log[PD_S\,(R_H)]_{kl} = A + B \bullet\ log(M_0)_k + w_j C_j + (1 - w_j)\, C_{j+1} + \sum_{i=1}^{N_{sta}} \delta_{il} S_i \tag{1}$$

and

$$log[IV2_S\,(R_H)]_{kl} = D + F \bullet\ log(E_S)_k + w_j G_j + (1 - w_j)\, G_{j+1} + \sum_{i=1}^{N_{sta}} \delta_{il} Z_i \tag{2}$$

where, the hypocentral distance (R_H) range is discretized into N_{bin}; the index $j = 1,., N_{bin}$ indicates the *j*th node selected such that R_H is between the distances $r_j \le R_H < r_{j+1}$; the attenuation function is linearized between nodes r_j and r_{j+1} using the weights *w*, computed as $w_j = (r_{j+1} - R_H)/(r_{j+1} - r_j)$. The distance range 10–120 km is discretized into 50 bins equally spaced on a logarithmic scale. The S_i and Z_i terms are the station corrections for station *i*, and N_{sta} is the number of stations, where we constrain the station corrections to zero mean. The coefficients A, B, C_j, D, F, and G_j are determined by solving the over-determined linear systems (Eqs. 1 and 2) in a least-square sense.

To fix the trade-off between A and C_j, and as well D and G_j the attenuation is constrained to zero at R equal to 10 km. The calculated regressions have a R-squared correlation coefficient (R^2) equal to 0.87 in both cases.

The observed PD_S and $IV2_S$ values corrected for the source scaling A + B *log*(M_0) and D + F *log*(E_S), respectively, are compared with the attenuation models C_j and G_j in Figures (S10d) and (S10g). The good agreement of the decay with distance between model parameters and corrected data confirms that the attenuation models are very robust.

The station corrections S and Z are shown in Figures (S10e and S10h). The station corrections and the coefficients of the attenuation models are reported in Table S2 and S3, respectively (Supplemental Material).

Finally, Figures (S10f) and (S10i) show the comparison between the values M_0 and E_S, from Cataldi et al. (2025)[30], with the values obtained correcting $IV2_S$ and PD_S for attenuation effects as modeled through the C_j and G_j coefficients. These results suggest that the scaling coefficients A, B and D, F capture well the trend in the data over the entire energy and moment ranges.

Step 2. Energy index

The RAMONES procedure is then applied to the 9,249 earthquakes and the obtained seismic moment, M_0, and radiated energy, E_S, estimates are used to calibrate a backbone scaling model relating log(M_0) and log(E_S), which serves as a reference for subsequent analyses, as follows:

$$\log(\mathrm{E_S}) = a \log(\mathrm{M_0}) + b, \tag{3}$$

where a is equal to 1.44 (± 0.04) and b is equal to − 10.92 (± 0.004), with residuals standard deviation equal to 0.3 and R^2 equal to 0.91 (Fig. 2a).

The Energy Index, EI, is then simply computed as the difference between the experimental E_S estimates (E_{Sobs}) and the predictions from the reference $E_S - M_0$ model (E_{Spr}, Eq. 3), where the input is the seismic moment M_0 from recorded earthquakes.

$$\mathrm{EI} = \log\ (\mathrm{E_{Sobs}}) - \log\ (\mathrm{E_{Spr}}) = \log\ (\mathrm{E_{Sobs}}) - -(\mathrm{a}\ \log\ (\mathrm{M_{0obs}}) + \mathrm{b}), \tag{4}$$

Positive (and negative) EI values indicate events radiating more (less) energy per unit-slip and unit-area (i.e., M_0) than expected by the model (Eq. 3).

Moment rate

To estimate the moment rate, we consider equally spaced longitude bins, each 0.25 degrees wide. We also consider earthquakes with a magnitude greater than the completeness magnitude (Mc). We compute $\dot{M}_0$ for each longitude bin and time window ΔT as follows[64]:

$$\dot{M}_0 = \frac{\sum M_0}{(\Delta T \cdot\ A)} \tag{5}$$

where the spatial extension A is estimated as the convex hull of the epicenters of events that occurred within the time window ΔT.

Data availability

All data generated or analysed during this study are included as supplemental material.The waveforms used in this work were provided by the following networks: [CH] Swiss Seismological Service (SED) At ETH Zurich. (1983). National Seismic Networks of Switzerland. ETH Zürich. [https://doi.org/10.12686/sed/networks/ch](https:/doi.org/10.12686/sed/networks/ch)[IT] Presidency of Council of Ministers—Civil Protection Department. (1972). Italian Strong Motion Network [Data set]. International Federation of Digital Seismograph Networks. [https://doi.org/10.7914/SN/IT](https:/doi.org/10.7914/SN/IT)[IV] Istituto Nazionale di Geofisica e Vulcanologia (INGV). (2005). Rete Sismica Nazionale (RSN) [Data set]. Istituto Nazionale di Geofisica e Vulcanologia (INGV). [https://doi.org/10.13127/sd/x0fxnh7qfy](https:/doi.org/10.13127/sd/x0fxnh7qfy)[MN] MedNet Project Partner Institutions. (1990). Mediterranean Very Broadband Seismographic Network (MedNet) [Data set]. Istituto Nazionale di Geofisica e Vulcanologia (INGV). [https://doi.org/10.13127/sd/fbbbtdtd6q](https:/doi.org/10.13127/sd/fbbbtdtd6q)[NI] OGS (Istituto Nazionale di Geofisica e di Geofisica Sperimentale) and University of Trieste. (2002). North-East Italy Broadband Network [Data set]. International Federation of Digital Seismograph Networks. [https://doi.org/10.7914/SN/NI](https:/doi.org/10.7914/SN/NI)[OE] ZAMG - Zentralanstalt für Meterologie und Geodynamik. (1987). Austrian Seismic Network [Data set]. International Federation of Digital Seismograph Networks. [https://doi.org/10.7914/SN/OE](https:/doi.org/10.7914/SN/OE)[OX] Istituto Nazionale di Oceanografia e di Geofisica Sperimentale—OGS. (2016). North-East Italy Seismic Network [Data set]. FDSN. [https://doi.org/10.7914/SN/OX](https:/doi.org/10.7914/SN/OX)[RF] University of Trieste. (1993). Friuli Venezia Giulia Accelerometric Network [Data set]. International Federation of Digital Seismograph Networks. [https://doi.org/10.7914/SN/RF](https:/doi.org/10.7914/SN/RF)[SI] ZAMG - Zentralanstalt für Meterologie und Geodynamik. Province Südtirol. [https://www.fdsn.org/networks/detail/SI/](https:/www.fdsn.org/networks/detail/SI)[SL] Slovenian Environment Agency (1990). Seismic Network of the Republic of Slovenia [Data set]. International Federation of Digital Seismograph Networks. [https://doi.org/10.7914/SN/SL](https:/doi.org/10.7914/SN/SL)[ST] Geological Survey-Provincia Autonoma di Trento. (1981). Trentino Seismic Network [Data set]. International Federation of Digital Seismograph Networks. [https://doi.org/10.7914/SN/ST](https:/doi.org/10.7914/SN/ST)[Z3] AlpArray Seismic Network. (2015). AlpArray Seismic Network (AASN) temporary component. AlpArray Working Group. [https://doi.org/10.12686/alparray/z3_2015](https:/doi.org/10.12686/alparray/z3_2015)[ZO] Massa, M., Rizzo, A. L., Lorenzetti, A., Lovati, S., D'Alema, E., Puglia, R., Carannante, S., & Luzi, L. (2021). Rete di monitoraggio multiparametrico del Garda (Nord Italia) - PDnet (Version 1.0) [Data set]. Istituto Nazionale di Geofisica e Vulcanologia (INGV). [https://doi.org/10.13127/sd/yhcfomcbo_](https:/doi.org/10.13127/sd/yhcfomcbo_)The network OX and NI are part of the "Sistema di Monitoraggio terrestre dell'Italia Nord Orientale (SMINO)" (Bragato et al., 2021; https://smino.ogs.it) 58 , which is operated by Center for Seismological Research (CRS) as a part of the National Institute of Oceanography and Applied Geophysics–OGS.

Received: 27 August 2025; Accepted: 7 January 2026
Published online: 19 January 2026

References

1. Seeber, L. & Armbruster, J. G. Earthquakes as beacons of stress change. *Nature* **407** (6800), 69–72. https://doi.org/10.1038/35024055 (2000).
2. Stein, R. S. & Lisowski, M. The 1979 homestead Valley earthquake Sequence, california: control of aftershocks and postseismic deformation. *J. Geophys. Research: Solid Earth*. **88** (B8), 6477–6490. https://doi.org/10.1029/JB088iB08p06477 (1983).
3. Brodsky, E. E. The importance of studying small earthquakes, Tiny earthquakes stitch together big ones. *Science*. **364**(6442), https://doi.org/10.1126/science.aax2490 (2019).
4. Goebel, T. H. W., Hauksson, E., Shearer, P. M. & Ampuero, J. P. Stress-drop heterogeneity within tectonically complex regions: A case study of San gorgonio Pass, Southern California. *Geophys. J. Int.* **202** (1), 514–528. https://doi.org/10.1093/gji/ggv160 (2015).
5. Yamada, T., Saito, Y., Tanioka, Y. & Kawahara, J. Spatial pattern in stress drops of moderate-sized earthquakes on the Pacific plate off the south-east of Hokkaido, japan: implications for the heterogeneity of frictional properties. *Progress Earth Planet. Sci.* **4** (1), 38. https://doi.org/10.1186/s40645-017-0152-7 (2017).

6. Moyer, P. A., Boettcher, M. S., McGuire, J. J. & Collins, J. A. Spatial and Temporal variations in earthquake stress drop on Gofar transform fault, East Pacific rise: implications for fault strength. *J. Geophys. Research: Solid Earth*. **123** (9), 7722–7740. https://doi.org/10.1029/2018JB015942 (2018).
7. Picozzi, M. et al. Spatiotemporal evolution of microseismicity seismic source properties at the Irpinia Near-Fault Observatory, Southern Italy. *Bull. Seismol. Soc. Am.* **112** (1), 226–242. https://doi.org/10.1785/0120210064 (2022a).
8. Picozzi, M., Spallarossa, D., Bindi, D., Iaccarino, A. G. & Rivalta, E. Detection of spatial and temporal stress changes during the 2016 central italy seismic sequence by monitoring the evolution of the energy index. *Journal of Geophysical Research: Solid Earth*. **127**(11), eJB025100 https://doi.org/10.1029/2022JB025100 (2022).
9. Chen, X. et al. Stress drop variations of (A)Seismic fault segments in the sea of Marmara region (Northwestern Türkiye) supported by different methodological approaches. *Bull. Seismol. Soc. Am.* **115** (3), 1016–1030. https://doi.org/10.1785/0120240128 (2025).
10. Bindi, D., Cotton, F., Spallarossa, D., Picozzi, M. & Rivalta, E. Temporal variability of ground shaking and stress drop in central italy: A hint for fault healing? *Bull. Seismol. Soc. Am.* **108** (4), 1853–1863. https://doi.org/10.1785/0120180078 (2018).
11. Toker, M. Symptomatic discretization of small earthquake clusters reveals seismic coupling to 2017 Bodrum earthquake (M_w 6.6) in the Gulf of Gökova (SW-corner of Turkey): Viscous-compliant seismogenesis over back-arc setting. *J. Afr. Earth Sc.* **177**, 104156 (2021).
12. Toker, M., Yavuz, E., Utkucu, M. & Uzunca, F. Multiple segmentation and seismogenic evolution of the 6th February 2023 (M_w 7.8 and 7.7) consecutive earthquake ruptures and aftershock deformation in the Maras triple junction region of SE-Anatolia, Turkey, physics of the Earth and planetary Interiors, v. 345, 107114, ISSN 0031–9201, (2023). https://doi.org/10.1016/j.pepi.2023.107114
13. Becker, D., Martínez-Garzón, P., Wollin, C., Kılıç, T. & Bohnhoff, M. Variation of fault creep along the overdue Istanbul-Marmara seismic gap in NW Türkiye. *Geophys. Res. Lett.* 50. https://doi.org/10.1029/2022GL101471 (2023).
14. Bressan, G., Bragato, P. L. & Venturini, C. Stress and strain tensors based on focal mechanisms in the seismotectonic framework of the Friuli-Venezia Giulia region (Northeastern Italy). *Bull. Seismol. Soc. Am.* **93** (3), 1280–1297. https://doi.org/10.1785/0120020058 (2003).
15. Viganò, A. et al. Earthquake relocations, crustal rheology, and active deformation in the central–eastern alps (N Italy). *Tectonophysics* **661**, 81–98. https://doi.org/10.1016/j.tecto.2015.08.017 (2015).
16. Šket Motnikar, B. et al. The 2021 seismic hazard model for Slovenia (SHMS21): overview and results. *Bulletin of Earthquake Engineering (2022)* **20**, 4865–4894 https://doi.org/10.1007/s10518-022-01399-8 (2022).
17. Guidoboni, E., Comastri, A. & Boschi, E. The exceptional earthquake of 3 January 1117 in the Verona area (northern Italy): A critical time review and detection of two lost earthquakes (lower Germany and Tuscany). *J. Geophys. Research: Solid Earth.* **110** (B12), JB003683 https://doi.org/10.1029/2005JB003683 (2005).
18. Caracciolo, C. H., Slejko, D., Camassi, R. & Castelli, V. The Eastern alps earthquake of 25 January 1348: new insights from old sources. *Bull. Geophys. Oceanogr.* **63** (3), 335–364. https://doi.org/10.4430/bgo00364 (2021).
19. Guidoboni, E. et al. CFTI5Med, the new release of the catalogue of strong earthquakes in Italy and in the mediterranean area. *Sci. Data*. **6** (1), 80. https://doi.org/10.1038/s41597-019-0091-9 (2019).
20. Fitzko, F., Suhadolc, P., Aoudia, A. & Panza, G. F. Constraints on the location and mechanism of the 1511 Western-Slovenia earthquake from active tectonics and modeling of macroseismic data. *Tectonophysics* **404** (1–2), 77–90. https://doi.org/10.1016/j.tecto.2005.05.003 (2005).
21. Slejko, D., Neri, G., Orozova, I., Renner, G. & Wyss, M. Stress field in Friuli (NE Italy) from fault plane solutions of activity following the 1976 main shock. *Bull. Seismol. Soc. Am.* **89** (4), 1037–1052. https://doi.org/10.1785/BSSA0890041037 (1999).
22. Villani, F., Antonioli, A., Pastori, M., Baccheschi, P. & Ciaccio, M. G. Stress patterns and crustal anisotropy in the Eastern alps: insights from seismological and geological observations. *Tectonics* **43** (3), e2023TC008033. https://doi.org/10.1029/2023TC008033 (2024).
23. Spallarossa, D. et al. The RAMONES service for rapid assessment of seismic moment and radiated energy in central italy: Concepts, Capabilities, and future perspectives. *Seismol. Res. Lett.* **92** (3), 1759–1772. https://doi.org/10.1785/0220200348 (2021).
24. Castro, R. R., Pacor, F., Sala, A. & Petrungaro, C. S wave attenuation and site effects in the region of Friuli. *Italy J. Geophys. Res.* **101** (B10), 22355–22369 https://doi.org/10.1029/96JB02295 (1996).
25. Malagnini, L., Akinci, A., Herrmann, R., Pino, N. & Scognamiglio, L. Characteristics of the ground motion in Northeastern Italy. *Bull. Seism Soc. Am.* **92**, 2186–2204. https://doi.org/10.1785/0120010219 (2002).
26. Franceschina, G., Kravanja, S. & Bressan, G. Source parameters and scaling relationships in the Friuli-Venezia Giulia (Northeastern Italy) region. *Phys. Earth Planet. Inter*. **154** (2), 48–167. https://doi.org/10.1016/j.pepi.2005.09.004 (2006).
27. Restivo, A., Bressan, G. & Sugan, M. Stress and strain patterns in the Venetian Prealps (north-eastern Italy) based on focal-mechanism solutions. *Bollettino Di Geofis. Teorica E Appl.* **57** (1), 13–30 https://doi.org/10.4430/bgta0166 (2006).
28. Klin, P., Laurenzano, G., Barnaba, C., Priolo, E. & Parolai, S. Site amplification at permanent stations in Northeastern Italy. *Bull. Seism Soc. Am.* **111**, 1885–1904. https://doi.org/10.1785/0120200361 (2021).
29. Cataldi, L., Poggi, V., Costa, G., Parolai, S. & Edwards, B. Parametric spectral inversion of seismic source, path and site parameters: application to Northeast Italy. *Geophys. J. Int.* **232** (3), 1926–1943. https://doi.org/10.1093/gji/ggac431 (2023).
30. Cataldi, L. et al. Stress drop and seismic efficiency distributions over the Adriatic indenter (European Eastern Alps). *Journal Geophys. Research: Solid Earth* (2026). (**Under Review**).
31. McGarr, A. On relating apparent stress to the stress causing earthquake fault slip. *J. Geophys. Research: Solid Earth*. **104** (B2), 3003–3011. https://doi.org/10.1029/1998JB900083 (1999).
32. Bindi, D., Picozzi, M., Spallarossa, D., Cotton, F. & Kotha, S. R. Impact of magnitude selection on aleatory variability associated with Ground-Motion prediction equations: part II—Analysis of the Between-Event distribution in central Italy. *Bull. Seismol. Soc. Am.* **109** (1), 251–262. https://doi.org/10.1785/0120180239 (2019).
33. Picozzi, M. et al. Rapid determination of *P* wave-based energy magnitude: insights on source parameter scaling of the 2016 central Italy earthquake sequence. *Geophys. Res. Lett.* **44** (9), 4036–4045. https://doi.org/10.1002/2017GL073228 (2017).
34. Picozzi, M., Bindi, D., Spallarossa, D., Di Giacomo, D. & Zollo, A. A rapid response magnitude scale for timely assessment of the high frequency seismic radiation. *Sci. Rep.* **8** (1), 8562. https://doi.org/10.1038/s41598-018-26938-9 (2018).
35. Picozzi, M. et al. Moment and energy magnitudes: diversity of views on earthquake shaking potential and earthquake statistics. *Geophys. J. Int.* **216** (2), 1245–1259. https://doi.org/10.1093/gji/ggy488 (2019a).
36. Picozzi, M., Bindi, D., Zollo, A., Festa, G. & Spallarossa, D. Detecting long-lasting transients of earthquake activity on a fault system by monitoring apparent stress, ground motion and clustering. *Sci. Rep.* **9** (1), 16268. https://doi.org/10.1038/s41598-019-52756-8 (2019b).
37. Brown, L. & Hudyma, M. Identification of stress change within a rock mass through apparent stress of local seismic events. *Rock Mech. Rock Eng.* **50** (1), 81–88. https://doi.org/10.1007/s00603-016-1092-z (2017).
38. Picozzi, M., Spallarossa, D., Iaccarino, A. G. & Bindi, D. Temporal evolution of radiated energy to seismic moment scaling during the preparatory phase of the M_w 6.1, 2009 l'aquila earthquake (Italy). *Geophys. Res. Lett.* **49** (8), e2021GL097382. https://doi.org/10.1029/2021GL097382 (2022c).
39. Kanamori, H. The energy release in great earthquakes. *J. Phys. Res.* **82** (20), 2981–2987. https://doi.org/10.1029/JB082i020p02981 (1977).
40. Hanks, T. C. & Kanamori, H. A moment magnitude scale. *J. Geophys. Research: Solid Earth*. **84** (B5), 2348–2350. https://doi.org/10.1029/JB084iB05p02348 (1979).

41. Wiemer, S. Minimum magnitude of completeness in earthquake catalogs: examples from Alaska, the Western united States, and Japan. *Bull. Seismol. Soc. Am.* **90** (4), 859–869. https://doi.org/10.1785/0119990114 (2000).
42. Woessner, J. Assessing the quality of earthquake catalogues: estimating the magnitude of completeness and its uncertainty. *Bull. Seismol. Soc. Am.* **95** (2), 684–698. https://doi.org/10.1785/0120040007 (2005).
43. Gutenberg, B. & Richter, C. F. Earthquake magnitude, intensity, energy, and acceleration*. *Bull. Seismol. Soc. Am.* **32** (3), 163–191. https://doi.org/10.1785/BSSA0320030163 (1942).
44. Aki, K. Maximum likelihood estimate of b in the formula log10N = a-bm and its confidence limits. *Bull. Earthq. Res.* **43**, 237–239 (1965).
45. Efron, B. Bootstrap methods: another look at the jackknife. *Annals Stat.* **7** (1). https://doi.org/10.1214/aos/1176344552 (1979).
46. Picozzi, M. et al. Spatiotemporal evolution of Ground-Motion intensity at the Irpinia Near-Fault Observatory, Southern Italy. *Bull. Seismol. Soc. Am.* **112** (1), 243–261. https://doi.org/10.1785/0120210153 (2021).
47. Ester, M., Kriegel, H. P., Sander, J. & Xu, X. A density-based algorithm for discovering clusters in large spatial databases with noise. *Proceedings of the Second International Conference on Knowledge Discovery and Data Mining (KDD'96)*, 226–231. (1996).
48. Kanamori, H. & Heaton, T. H. Geophysical Monograph Series. In: *Microscopic and macroscopic physics of earthquakes*. (Vol. 120), 147–163 (eds Rundle, J. B., Turcotte, D. L. & Klein, W.) (American Geophysical Union, 2000). https://doi.org/10.1029/GM120p0147 (2000).
49. Zúñiga, F. R. & Rodríguez-Pérez, Q. Stress differences and their role in identifying earthquake source process properties at different tectonic environments. *J. Seismolog.* **29** (2), 337–352. https://doi.org/10.1007/s10950-025-10286-z (2025).
50. Orowan, E. Chapter 12: Mechanism of Seismic Faulting. In Geological Society of America Memoirs (Vol. 79, 323–346). Geological Society of America. https://doi.org/10.1130/MEM79-p323 (1960).
51. DISS Working Group. *Database of Individual Seismogenic Sources (DISS), version 3.3.0: A compilation of potential sources for earthquakes larger than M 5.5 in Italy and surrounding areas*. (Version 3.3.0) Istituto Nazionale di Geofisica e Vulcanologia (INGV). (2021). https://doi.org/10.13127/DISS3.3.0
52. Jozi Najafabadi, A., Haberland, C., Handy, M. R., Le Breton, E. & Weber, M. Seismic wave Attenuation (1/Qp) in the crust underneath the Eastern and Eastern Southern alps (Europe): imaging effects of faults, fractures, and fluids. *Earth Planet Space*. **75** (1), 187. https://doi.org/10.1186/s40623-023-01942-0 (2023).
53. Cheloni, D., D'Agostino, N. & Selvaggi, G. Interseismic coupling, seismic potential, and earthquake recurrence on the Southern front of the Eastern alps (NE Italy). *J. Geophys. Research: Solid Earth*. **119** (5), 4448–4468. https://doi.org/10.1002/2014JB010954 (2014).
54. Serpelloni, E., Vannucci, G., Anderlini, L. & Bennett, R. A. Kinematics, seismotectonics and seismic potential of the Eastern sector of the European alps from GPS and seismic deformation data. *Tectonophysics* **688**, 157–181. https://doi.org/10.1016/j.tecto.2016.09.026 (2016).
55. Viganò, A., Scafidi, D., Martin, S. & Spallarossa, D. - Structure and properties of the Adriatic crust in the central-eastern Southern alps (Italy) from local earthquake tomography. *Terra Nova*. **25**, 504–512 (2013).
56. Bressan, G., Gentile, G. F., Tondi, R., De Franco, R. & Urban, S. Sequential Integrated Inversion of tomographic images and gravity data: an application to the Friuli area (north-eastern Italy). *Bollettino di Geofis. Teorica ed. Appl.* **53** (2), 191–212 https://doi.org/10.4430/bgta0059 (2012).
57. Rovida, A. et al. Italian Parametric Earthquake Catalogue (CPTI15), version 4.0 [Data set]. Istituto Nazionale di Geofisica e Vulcanologia (INGV). https://doi.org/10.13127/cpti/cpti15.4 (2022).
58. Bragato, P. L. et al. The OGS– Northeastern Italy seismic and deformation network: current status and outlook. *Seismol. Res. Lett.* **92**, 1704–1716. https://doi.org/10.1785/0220200372 (2021).
59. Petersen, G. M., Hofman, L. J., Kummerow, J. & Cesca, S. Microseismicity in the Large-N Swath-D network: revealing seismic sequences and active faults in the Eastern alps. *J. Geophys. Research: Solid Earth*. **130** (2), e2024JB030516. https://doi.org/10.1029/2024JB030516 (2025).
60. Vuan, A. et al. NITRO (North-Eastern Thrust Faults Observatory), Conference: SLOVENIA – NFO Meeting, November 2019, https://doi.org/10.13140/RG.2.2.11327.12964 (2019).
61. Viganò, A., Ranalli, G., Andreis, D. & Martin, S. Inversion for the static friction coefficient of seismogenic faults: application to induced seismicity of the Basel enhanced geothermal System, Switzerland. *J. Geodyn.* **145**, 101843. https://doi.org/10.1016/j.jog.2021.101843 (2021).
62. Picozzi, M., Iaccarino, A. G., Spallarossa, D. & Bindi, D. On catching the preparatory phase of damaging earthquakes: an example from central Italy. Sci. Rep. **2023**, https://doi.org/10.1038/s41598-023-41625-0 (2023).
63. Picozzi, M., Iaccarino, A. G. & Spallarossa, D. The Preparatory Process of the 2023 M_w 7.8 Türkiye Earthquake. Sci. Rep. https://doi.org/10.1038/s41598-023-45073-8 (2024).
64. Picozzi, M., Spallarossa, D., Iaccarino, A. G. & Bindi, D. Event-specific ground motion anomalies highlight the preparatory phase of earthquakes during the 2016–2017 Italian seismicity. *Commun. Earth Environ.* **2024** (5), 289 https://doi.org/10.1038/s43247-024-01455-y (2024).
65. Scafidi, D. et al. A complete automatic procedure to compile reliable seismic catalogs and Travel-Time and Strong-Motion parameters datasets. *Seismol. Res. Lett.* **90** (3), 1308–1317. https://doi.org/10.1785/0220180257 (2019).
66. Lomax, A., Virieux, J., Volant, P. & Berge-Thierry, C. Probabilistic Earthquake Location in 3D and Layered Models. In: *Advances in Seismic Event Location* (eds Thurber, C. H. & Rabinowitz, N.) (Vol. 18, pp. 101–134). https://doi.org/10.1007/978-94-015-9536-0_5 (Springer Netherlands, 2000)
67. Di Bona, M. A local magnitude scale for crustal earthquakes in Italy. *Bull. Seismol. Soc. Am.* **106** (1), 242–258. https://doi.org/10.1785/0120150155 (2016).
68. Riggio, A. & Russi, M. Procedura Di analisi ed elaborazione dei Dati registrati Da reti Sismometriche locali. Finalità Ed. Esperienze Della Rete Sismometrica Del. FVG, 53–74. (1984).

Acknowledgements

This research was supported by the PRIN 2022 project '2022ZHXWC9'—Intercepting the PREparatory Phase of lARge earthquakes from seismic information and gEodetic Displacement (PREPARED).This study was partially funded by the Joint Research Unit (JRU) of European Plate Observing System infrastructure (EPOS) Italia (https://www.epos-italia.it/, last accessed September 2024).

Author contributions

MP was responsible for conceiving and designing the work. DS and DB contributed to its conception. DS acquired and analysed the data. MP performed the analyses for energy index estimation and interpretation. All authors contributed to interpreting the results and writing the manuscript.

Funding

This research was supported by the PRIN 2022 project '2022ZHXWC9'—Intercepting the PREparatory Phase of

lARge earthquakes from seismic information and gEodetic Displacement (PREPARED).

Declarations

Competing interests
The authors declare no competing interests.

Additional information
Supplementary Information The online version contains supplementary material available at https://doi.org/10.1038/s41598-026-35618-y.

Correspondence and requests for materials should be addressed to M.P.

Reprints and permissions information is available at www.nature.com/reprints.

Publisher's note Springer Nature remains neutral with regard to jurisdictional claims in published maps and institutional affiliations.